Assessing inversion uncertainty from initial model variability: A practical approach for geothermal MT exploration

Atsushi Suzuki[a]*

[a] *JX Metals Resources Exploration & Development Co., Ltd., Tokyo, Japan*

address: 1-9, Kanda Nishikicho, Chiyoda-Ku, Tokyo 101-0054, Japan

e-mail: suzuki@tankai.co.jp

Assessing inversion uncertainty from initial model variability: A practical approach for geothermal MT exploration

Abstract

We propose a simple and computationally efficient approach to evaluate the uncertainty in magnetotelluric (MT) inversion results arising from differences in initial models. Spatially smooth initial resistivity structures are generated by assigning random resistivity values to fixed representative points and applying Kriging-based interpolation. A series of 3D inversions was conducted using these initial models, and the variability in the resulting resistivity distributions was analyzed. Results from field data acquired in the Yuzawa geothermal field (northeastern Japan) demonstrate that even when using the same dataset and inversion parameters, the final resistivity models exhibit meaningful variability depending on the initial model. The selected cases with final RMS values ≤ 2.15 reveal spatial patterns in uncertainty: the smaller-area realizations were entirely encompassed within the larger-area realizations at a depth of 1000 m, indicating a conductive core region that is common to all realizations, while the spatial extent of C1 became more variable among realizations in the eastern region with increasing depth, reflecting greater uncertainty. This spatially variable uncertainty can guide the planning of drilling and geophysical surveys. Furthermore, the distribution of isosurface volumes below a given resistivity threshold enables the construction of optimistic and pessimistic scenarios for reservoir modeling. The proposed approach is scalable and well-suited for practical geothermal applications where efficient and feasible uncertainty assessment is required. This method provides a practical framework for evaluating geothermal potential.

Keywords: Magnetotellurics, 3D inversion, initial model, uncertainty analysis, geothermal exploration, Kriging

Highlights

- Simple workflow quantifies MT inversion uncertainty from initial model variability.
- Shallow conductive core is consistent; deeper anomaly becomes uncertain eastward.
- Ensemble approach with Kriging provides scalable, parallelizable uncertainty analysis.
- Results guide drilling target selection and support scenario-based reservoir modeling.
- Practical framework demonstrates feasibility of incorporating uncertainty in MT workflows.

Introduction

Magnetotellurics (MT) is a geophysical method used to image subsurface resistivity structures. It has been widely applied in Earth sciences and resource exploration, including geothermal and mineral investigations. In recent years, three-dimensional (3D) MT inversion has become increasingly common, enabling both qualitative and quantitative estimation of subsurface resistivity, due to advances in computational power and inversion algorithms (e.g., Ishizu et al., 2022; Usui et al., 2024).

Theoretically, quantitative subsurface resistivity distributions can be estimated from surface-acquired MT data by minimizing an objective function that incorporates both data misfit and regularization constraints (Kelbert et al., 2014; Sasaki, 2004; Siripunvaraporn et al., 2005; Usui, 2015). However, 3D inversion poses several challenges. First, it requires repeated solutions of the forward problem, which numerically simulates electromagnetic wave propagation and is computationally intensive. Additionally, MT inversion is an ill-posed problem, as the number of data is typically much smaller than the number of model parameters (cells) used in the forward modeling. As a result, the inversion outcome depends strongly on the initial model and represents only one solution among infinitely many possible ones (Muñoz & Rath, 2006; Páll Hersir et al., 2013; Robertson et al., 2020). Therefore, inversion requires both high computational cost and careful evaluation of solution uncertainty. Although some studies have attempted to assess this uncertainty (Robertson et al., 2020; Rung-Arunwan et al., 2022), such evaluations remain uncommon due to the associated computational demands.

Recently, Suzuki (2025) developed an efficient MT inversion program that addresses some of these challenges. Their approach employs an iterative solver for the forward problem and uses the adjoint-state method to compute the gradient of the objective function for model updates. In their study, they successfully solved a practical-scale problem (~250,000 cells) within approximately one day on a workstation-class computer. This improvement in computational efficiency makes it more feasible to explore practical methods for evaluating inversion uncertainty, which has been limited so far.

The evaluation of inversion uncertainty is crucial for improving the reliability of MT interpretation. In geothermal development, MT surveys are frequently used to identify conductive zones that may correspond to hydrothermal reservoirs, cap rocks, or supercritical fluids. Since drilling costs are high and geological conditions are complex, robust assessment of resistivity model uncertainty is essential for minimizing economic risks and for optimizing the siting of production or injection wells. Therefore, practical and computationally efficient methods for uncertainty evaluation are directly relevant to decision-making in geothermal resource exploration and development.

Further, it also enables more rigorous and quantitative comparisons between inversion results and experimental data or measurements (Iwamori et al., 2021; Takakura & Nakayama, 2017), which typically include value ranges or uncertainties, contributing to more robust model validation and interpretation accuracy.

To address this issue, the present study investigates the variability in inversion results caused by differences in initial models using actual MT field data. A simple and computationally efficient approach is proposed to evaluate uncertainty, aiming to provide a foundation for future practical applications of 3D MT inversion.

Methodology

Initial Model Generation

We define the initial model dependence problem as:

$$\boldsymbol{m}(\boldsymbol{m_0}) = \arg\min_{m^*} F(\boldsymbol{m}^*, \boldsymbol{m_0}) \tag{1}$$

where $\boldsymbol{m_0} \in \mathbb{R}^N$ is an initial guess of the model parameters, N is the number of the model parameters, F is the objective function, and $\boldsymbol{m}(\boldsymbol{m_0})$ denotes the inversion result obtained from a given initial guess. The uncertainty due to different initial guesses can be evaluated from the ensemble of models $\boldsymbol{m}(\boldsymbol{m_0})$.

To efficiently obtain such an ensemble from the relevant parameter space, prior information—such as known geological structures or results from other geophysical methods—can be incorporated to define plausible resistivity ranges and generate initial models accordingly(Causse, 2023). However, MT is often used in preliminary surveys (e.g., Ogawa et al., 1997) during resource exploration or to image structures deeper than the reach of drilling (e.g., Ichiki et al., 2021; Zhang et al., 2025). In such cases, feasible resistivity ranges are often unknown.

A common approach in MT to examine sensitivity to the initial model is to test a few homogeneous starting models with different resistivity values e(Robertson et al., 2020, Ishizu et al., 2022). However, this strategy explores only a very limited portion of the model parameter space. To obtain a broader understanding of inversion behaviour, we must explore a wider range of initial models.

One of the simplest approaches under this condition is to assign random resistivity values to each model cell. However, this method tends to introduce abrupt resistivity changes between neighboring cells, which can lead to numerical instability in the inversion. Moreover, the degrees of freedom in defining the initial model become excessively large, making the exploration of the parameter space inefficient.

To address these issues, we propose a hybrid approach based on the use of representative points and spatial interpolation and extrapolation. The algorithm consists of the following steps:

(1) Select representative points covering both the survey area and depth of interest,

(2) Assign random resistivity values within a reasonable range to these points,

(3) Use Kriging (Isaaks and Srivastava, 1989) to interpolate and extrapolate the values to all model cells used in the forward modeling,

(4) Run the inversion using the generated initial model,

(5) Repeat steps (2) through (4),

(6) Evaluate the resulting ensemble of models $\boldsymbol{m}(\boldsymbol{m_0})$ to quantify uncertainty.

This method reduces the dimensionality of the initial model space and enables more efficient exploration. Although simple, it provides flexibility in the selection and distribution of representative points. The proposed approach is conceptually similar to the use of "pilot points" in PEST, a model-independent parameter estimation and uncertainty analysis framework (Doherty et al., 2011). The method is also highly parallelizable, as each inversion is independent of the others. Therefore, near-linear speed-up can be expected with increasing numbers of computing nodes. The flowchart of this method is shown in Figure 1.

Bayesian approaches, such as Markov chain Monte Carlo (MCMC) methods, have been widely used to quantify uncertainty in geophysical inversion by sampling the posterior distribution around a particular solution (Manassero et al., 2020). Similarly, sensitivity analyses (e.g., Ichihara et al., 2014; Pace et al., 2022) investigate how local perturbations in model parameters or data affect the inversion outcome, typically assuming that the selected solution is reasonably close to the true structure. However, the present study addresses a different aspect of uncertainty—namely, the variability in inversion outcomes caused by differences in initial models. This reflects a practical form of ambiguity commonly encountered in 3D MT inversion workflows. While our method does not provide a formal posterior distribution or sensitivity map, it highlights the range of plausible resistivity structures that may arise solely from changes in the initial model, independent of observational noise, regularization choices, or prior structural assumptions.

MT Inversion.

MT inversion in our case uses the impedance tensor Z and the tipper **T** as below:

$$\begin{pmatrix} E_x \\ E_y \end{pmatrix} = \begin{pmatrix} Z_{xx} & Z_{xy} \\ Z_{yx} & Z_{yy} \end{pmatrix} \begin{pmatrix} H_x \\ H_y \end{pmatrix}, \tag{2}$$

$$H_z = \begin{pmatrix} T_x & T_y \end{pmatrix} \begin{pmatrix} H_x \\ H_y \end{pmatrix} \tag{3}$$

where **E** is the electric fields, **H** is the magnetic field, $x, y,$ and z are the directions of the north–south, east–west, and vertical directions, respectively.

We define the objective function to match the calculated impedance tensor and the tipper with the calculated ones, as below:

$$F(\mathbf{m}) = |\mathrm{W}\mathbf{d}_{\mathbf{obs}} - \mathrm{W}\mathbf{d}_{\mathbf{calc}}|^2 + \alpha^2 |\mathrm{R}\log(\mathbf{m})|^2 + \beta^2 \sum_{n=1}^{N_{obs}} \sum_{i=1}^{2} \sum_{j=1}^{2} \left(D_{ij}^n - I_{ij}\right)^2 \tag{4}$$

where $\mathbf{m}$ is the model parameters, $\mathbf{d}_{\mathbf{obs}}$ and $\mathbf{d}_{\mathbf{calc}}$ are the observed and calculated data (i.e., components of the impedance tensor and tipper), W is the weight matrix, R is the smoothness matrix, D^n is the distortion tensor, I is the identity matrix, N_{obs} is the number of the observation sites, α^2 and β^2 is the trade-off parameters for the model smoothness constraint and estimation of the distortion tensor. Note that MT inversion is usually the ill-posed problem, hence the solution depends on the initial model parameters. The detailed explanation of the inversion scheme is written in Suzuki (2025).

Data and Settings

We used thirty MT data from (Ishizu et al., 2022), collected in Yuzawa, northeastern Japan, where several geothermal power plants are located (Figure 2). Ishizu et al. (2022) conducted an inversion with the same data and discussed the possible existence of a supercritical geothermal reservoir in this region based on MT inversion results.

As mentioned in the Introduction, we adopted the inversion code developed by Suzuki (2025). The model consisted of 34 × 34 × 62 cells (including 10 layers of air) along the north-south (X), east-west (Y), and vertical (Z) directions. A locally refined mesh was employed in the central part of the model to increase resolution in the area of interest. The total model extent was 200 km × 200 km × 160 km in the respective directions, with a total of 210,297 cells. The minimum cell sizes in the north-south, east-west, and vertical directions are 400 m, 400 m, and 30 m, respectively. We used constant resistivity in the air (10^6 Ω·m) and sea (0.25 Ω·m) layers. We considered the topography using ETOPO 2022 (Macferrin et al., 2025; NOAA National Centers for Environmental Information, 2022) with the unstructured hexahedral cells.

Four components of the impedance tensor and two components of the tipper were used in the inversion. We set the error floors of the impedance tensor and the tipper to 5% of $\left|Z_{xy}Z_{yx}\right|^{\frac{1}{2}}$ and 15% of absolute values of the components, respectively. These settings were the same as Ishizu et al. (2022). A map of the survey area and model setup is shown in Figure 2 and Figure 3. Twelve frequency points were used, ranging from 100 Hz to 0.001 Hz. The trade-off parameters α^2 and β^2, as defined in

Suzuki (2025), were set to the same value and successively reduced in the order of 10, 1, 0.1. We evaluated the final models when α^2 and β^2 equal to 0.1.

To generate the initial models, resistivity values at the representative points were randomly sampled on a $\log_{10}$ scale between 1 Ω·m and 1000 Ω·m. A total of 3 × 3 × 4 representative points were selected along the X, Y, and Z directions. The coordinates of the representative points were −10 km, 0 km, and 10 km in both X and Y directions. In the Z direction, representative points were selected at cell indices k = 11, 21, 31, and 41, where k denotes the cell index in the depth direction. Here, k = 11 corresponds to the topmost cell just below the air layer, i.e., the first cell beneath the surface. Because topography is included, the physical depth associated with a given k varies with (X,Y); accordingly, we refer to vertical levels by the index k —constant-elevation slices relative to the model datum—rather than by a single fixed depth below the local surface (Figure 3).

We used ordinary Kriging with an isotropic linear variogram (slope = 4,000; nugget = 0) to interpolate values from the representative points to all model cells. The slope was chosen as a pragmatic, grid-tied setting: a correlation length of ~10× the minimum horizontal cell size yielded spatially coherent initial models without oversmoothing. We did not attempt systematic optimization, prioritizing practical settings.

Inversions for each initial model were performed on four independent computers. The specifications of these machines are listed in Table 1. Note that these are standard workstation-level computers.

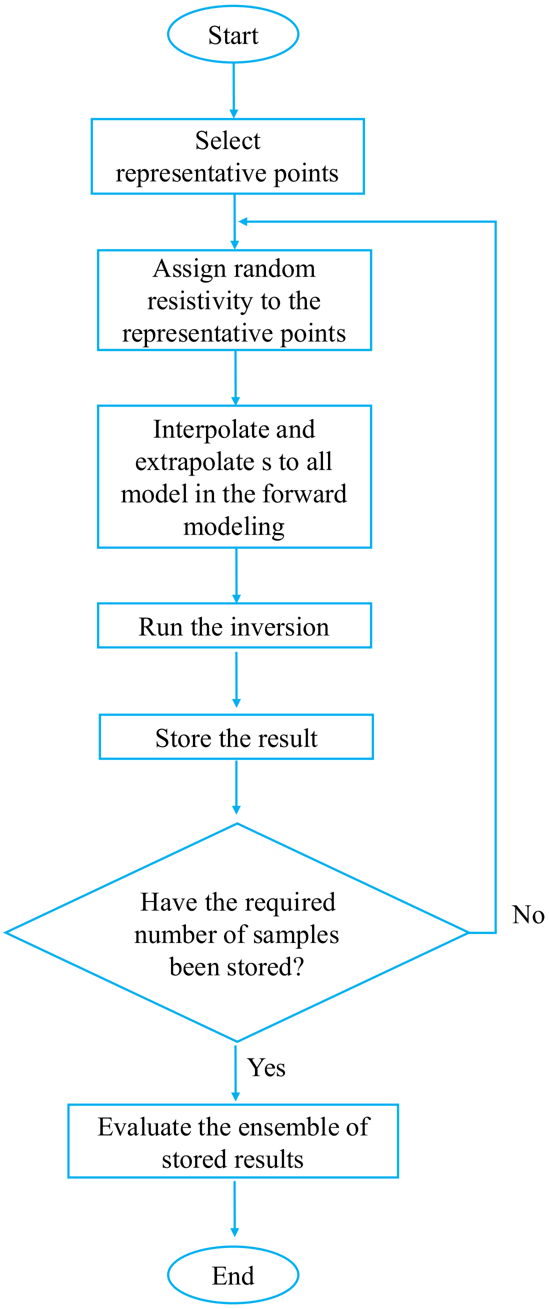

Figure 1

Flowchart illustrating the proposed approach for evaluating uncertainty arising from variations in initial models.

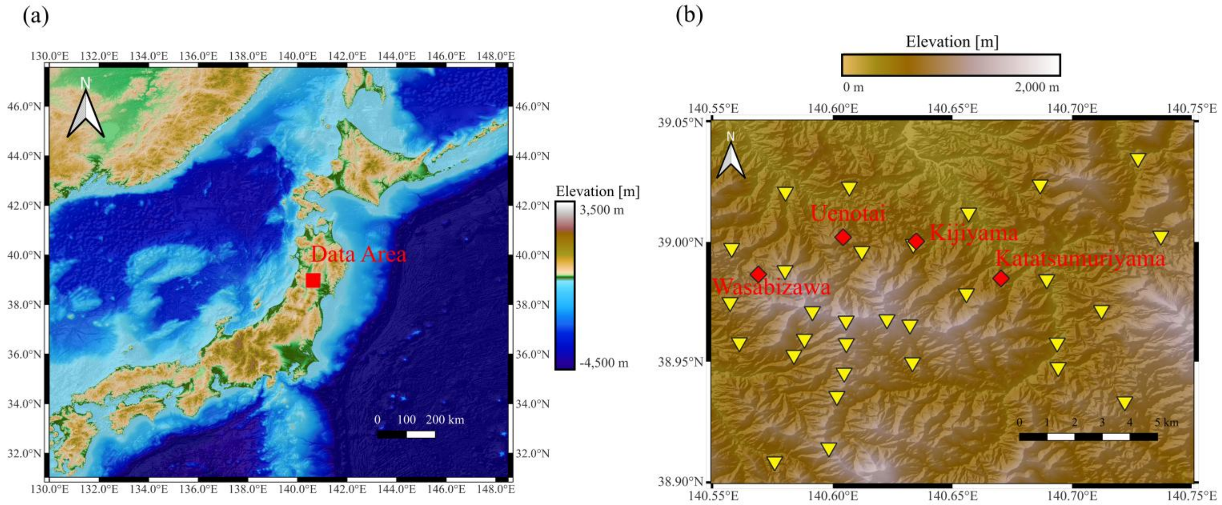

Figure 2

Maps showing (a) the broader region around Japan and (b) the study area.

Yellow triangles indicate MT observation sites, and red diamonds denote geothermal power plants either under construction or in operation. These maps were created using the GSI Fundamental Geospatial Data (Digital Elevation Model, 10 m mesh) (Geospatial Information Authority of Japan (GSI), 2025).

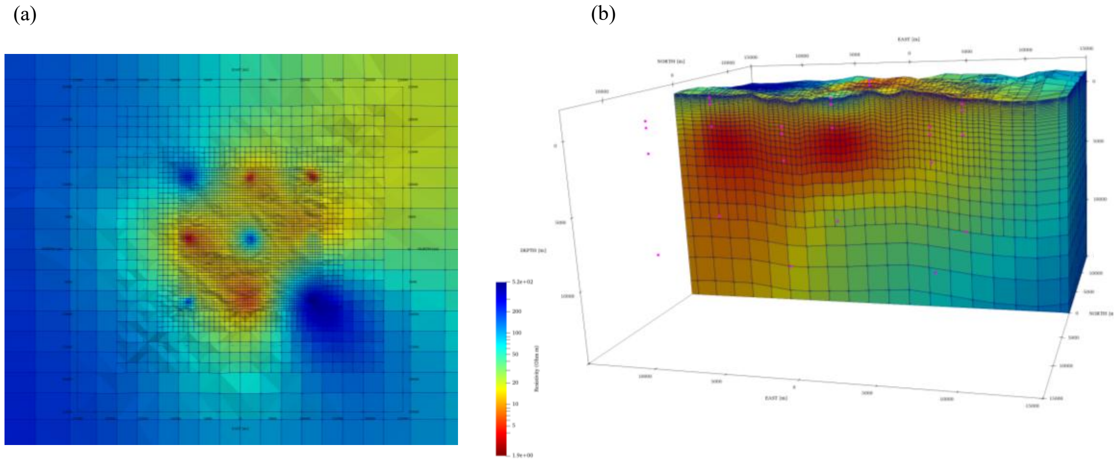

Figure 3

(a) Plan view and (b) oblique view of a sample generated initial model. Colors indicate resistivity, and blue lines outline the mesh cells. Pink points in (b) represent the representative points.

Table 1

Specifications of the computers and the required inversion times. The preprocessing time for preparing the input files (a few minutes per case) is not included in the total inversion time.

	CPU	Memory	Cases	Total Inversion Time (h)	Avg. Time / Case (h)	Notes
Run 1	Intel Core i7-9700	64GB	14	327.7	23.4	
Run 2	Intel Core i9-10900	64GB	18	345.5	19.2	
Run 3	Intel Core i7-14700	64GB	22	348.8	15.9	
Run 4	Intel Core i9-14900K	128GB	15	311.8	20.8	Run 4 and Run 5 were conducted in the same computer.
Run 5	Intel Core i9-14900K	128GB	18	315.1	17.5	

Results and Discussion

1. *Realization set and selection criteria*

We ran 87 3-D MT inversions with randomized initial models. Figure 4 shows the distribution of the final RMS values, which is bimodal, suggesting the presence of multiple local minima. From a data-fit perspective, we retained 48 realizations with RMS ≤ 2.15 as the better-fit subset (see Figure 4). We set the acceptance threshold at RMS = 2.15, chosen by visual inspection as the local minimum between the two modes in the final-RMS histogram (Figure 4).

Figure 5 shows the correlation between the initial and final RMS of the realizations. We find that they show little correlation, underscoring the need to explore diverse initial models.

2. *Ensemble-average structure and consistency checks*

The ensemble-average model—presented as a horizontal slice at 2500 m depth and two orthogonal vertical sections at X = 500 m and Y = 500 m (Figure 6) —captures the principal conductive body reported in previous studies (Ishizu et al., 2022).

3. *Overview using summary models*

To provide an overview (Figure 7), we present isosurfaces for the ensemble-average and the average ± 1σ models, where σ is the per-cell standard deviation of $\log_{10}$ ρ, where ρ denotes resistivity. For each realization, we computed ρ_{min} within the subvolume (X,Y: −4000–5000 m; Z: 0–5000 m) that contains the C1 anomaly. We then extracted the 3-D isosurface from the $\log_{10}\rho$ field at the level $L = \log_{10} \rho_{min} + 0.5$. This pragmatic choice reflects the logarithmic scaling typically used for resistivity: 0.5

in $\log_{10}$ corresponds to a mid-decade contrast (~3.16×). Tying the level to ρ_{min} helps reduce sensitivity to absolute resistivity level differences among realizations and enables direct, level-normalized comparison of extent and connectivity. The corresponding ρ_{min} are 4.0, 5.8, and 8.4 Ω·m for the −1σ, average, and +1σ cases, respectively. We set the isovalues relative to ρ_{min} rather than using a constant threshold (for example, 10 Ω·m) because a fixed threshold conflates geometric extent with absolute resistivity and hinders direct comparison across realizations. The isoisovalues are 12.7, 18.4, 26.7 Ω·m for average -1σ, average, and average +1σ cases, respectively.

Figure 8 shows cross-sections at depths of 1,000, 2,500, and 4,000 m for these three cases together with the per-cell standard deviations. Although the thresholds differ, the shallow isosurfaces are largely co-located and the standard deviation is small compared with the deeper region. In contrast, at depths of 2,500 and 4,000 m the isosurfaces diverge markedly in the eastern part of the model, which is also reflected in the higher standard deviation values. These patterns suggest that the position of the conductive region is relatively well constrained in the shallow section, whereas the geometry becomes increasingly uncertain toward the east at greater depths.

4. Cross-realization comparison using case-specific levels on slices

To compare realizations while reducing sensitivity to absolute resistivity offsets, we used the same operational level as in Section 3 but applied per realization to 2-D depth slices. Specifically, for each realization k we computed $\rho_{min,k}$ within the subvolume (X,Y: −4000–5000 m; Z: 0–5000 m) that contains the C1 anomaly, and then drew contours on the $\log_{10} \rho$ slices at the level

$$L_k = \log_{10} \rho_{min,k} + 0.5. \tag{5}$$

At 1000 m depth, the contours are largely nested, indicating a common shallow conductive core across realizations, although $\rho_{min,k}$ varies among cases. At 2,500–4,000 m, contour locations diverge and some realizations deviate from the trend defined by the majority (Figure 9 and Figure 10). The tendency for larger deviations in the east at 2,500 and 4,000 m appears to be driven mainly by these outlying realizations. Overall, geometric agreement is robust near the surface and in the western part of the model, but becomes increasingly uncertain toward the east at greater depths.

5. *Implications for Geothermal Exploration and Reservoir Modeling*

Inversion outcomes vary with the initial model and show depth-dependent divergence. Because resistivity is mapped to reservoir properties (e.g., porosity and fluid salinity via Archie-type relations), quantifying both amplitude variability and the geometry of conductive zones (volume/connectivity) is practically useful. The positional spread and deviation seen on depth slices (Figure 8, Figure 9 and Figure 10) identifies areas of agreement versus uncertainty. Taken together, this supports more informed decision-making in geothermal exploration—including drilling target selection and reservoir evaluation (e.g., Matsunaga & Kanda, 2025; Yokoi et al., 2025)—and contributes to more robust and transparent interpretation in practical geothermal development, especially by cautioning against over-interpretation of deeper features.

6. *Scope and limitations*

The variability quantified here arises from differences in initial models; other sources (data noise and errors, parametrization, structural constraints) are not treated.

The initial model parameterization uses 3 × 3 × 4 representative points on a regular lattice; we did not optimize their locations. Consequently, strong spatial anisotropy or layering not aligned with the lattice could bias the ensemble. A systematic study of point placement and density, in relation to the variogram ranges, is left for future work.

The computational requirements are also a key consideration for practical uncertainty analysis. Table 1 summarizes the inversion time on each computing system. In our environment, the total runtime was approximately 20 days, including interruptions due to system updates. This is considered practical, since magnetotelluric field data are typically acquired over periods of several months to years.

Although the current number of realizations is insufficient for a comprehensive statistical characterization of the parameter space, it is adequate for examining typical variability and identifying robust trends. Furthermore, the workflow is embarrassingly parallel, allowing the number of realizations—and thus the robustness of the statistical results—to be readily increased with additional computing resources.

Conclusion

This study proposed a simple and computationally efficient approach to evaluate the uncertainty in magnetotelluric (MT) inversion results caused by differences in initial models. To generate spatially coherent initial resistivity models, we used a small number of representative points with randomly assigned resistivity values and applied Kriging interpolation to construct smooth initial 3D resistivity structures.

Using these models, we performed multiple 3D inversions of the MT dataset presented by Ishizu et al. (2022), which was acquired in the Yuzawa geothermal field in Japan, and analyzed the variability of the resulting resistivity distributions. The results suggested that the final resistivity models can exhibit meaningful variability depending on the initial guess, even when using the same dataset and inversion settings.

The ensemble of selected cases (final RMS ≤ 2.15) provided insights into typical model variability and enabled an assessment of spatial uncertainty. In these realizations, the smaller-area realizations were entirely encompassed within the larger-area cases at a depth of 1000 m, indicating a conductive core region that is common to all realizations. In contrast, with increasing depth, the spatial extent of C1 became more variable among realizations in the eastern part of the model, reflecting greater uncertainty. Such information is valuable for geothermal exploration, as it can support decisions on drilling targets and guide the planning of supplementary geophysical surveys.

Furthermore, the method allows for the extraction of optimistic and pessimistic scenarios in reservoir modeling by evaluating the distribution of isosurface volumes below a given resistivity threshold. While the approach does not yield a formal probabilistic interpretation like Bayesian methods, it is scalable, parallelizable, and well-suited for practical applications where a feasible assessment of uncertainty is needed.

The proposed method provides a viable framework for quantifying inversion uncertainty due to initial model dependence in MT applications. By highlighting spatial patterns of variability in model outcomes, it supports more informed decision-making in geothermal exploration, including drilling target selection and reservoir evaluation, and contributes to more robust and transparent interpretation in practical geothermal development. This type of uncertainty assessment can also contribute to more realistic evaluations of geothermal potential, as emphasized by previous studies advocating for scenario-based interpretation and risk-informed decision-making in geothermal exploration (Witter et al., 2019).

It should be noted, however, that the uncertainty estimated by the proposed method represents a lower bound, as it is infeasible to exhaustively explore the entire initial model parameter space. Furthermore, other factors—such as data noise, inversion parameter settings, and structural constraints—can also significantly affect the final inversion results. Developing more efficient strategies for exploring the initial model space and incorporating these additional sources of uncertainty remain important directions for future work. Nevertheless, this study demonstrates the practical feasibility of incorporating initial model variability into routine MT interpretation workflows.

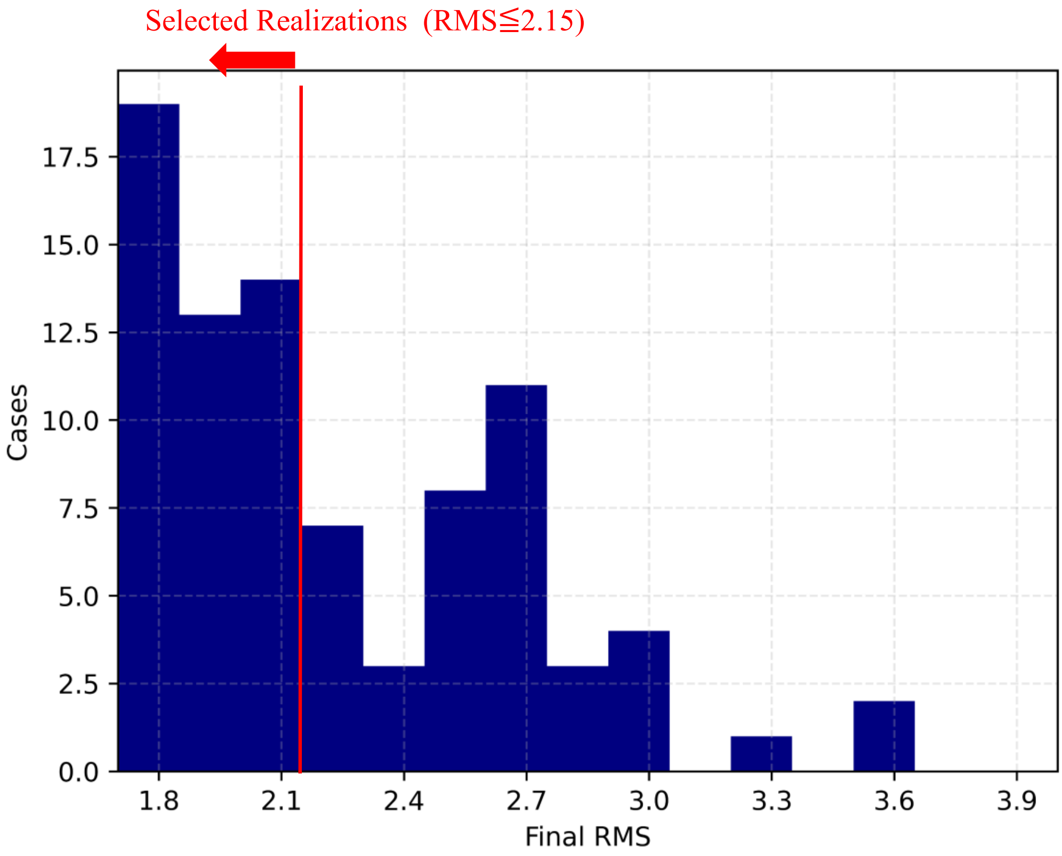

Figure 4

Histogram of final RMS values. Realizations with RMS values below 2.15 were selected for further analysis based on this distribution.

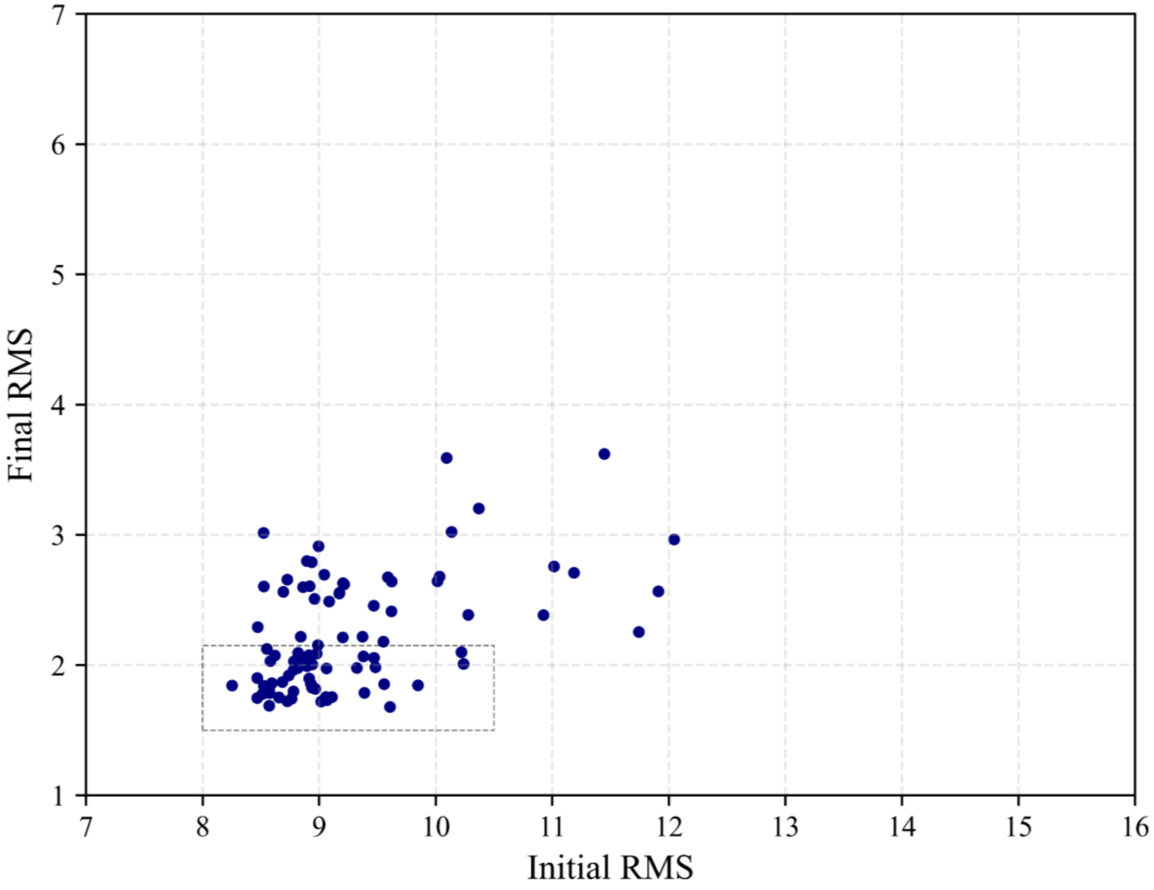

Figure 5

Scatter plot of initial versus final RMS values. The black dashed square indicates the selection region, where final RMS values are less than or equal to 2.15.

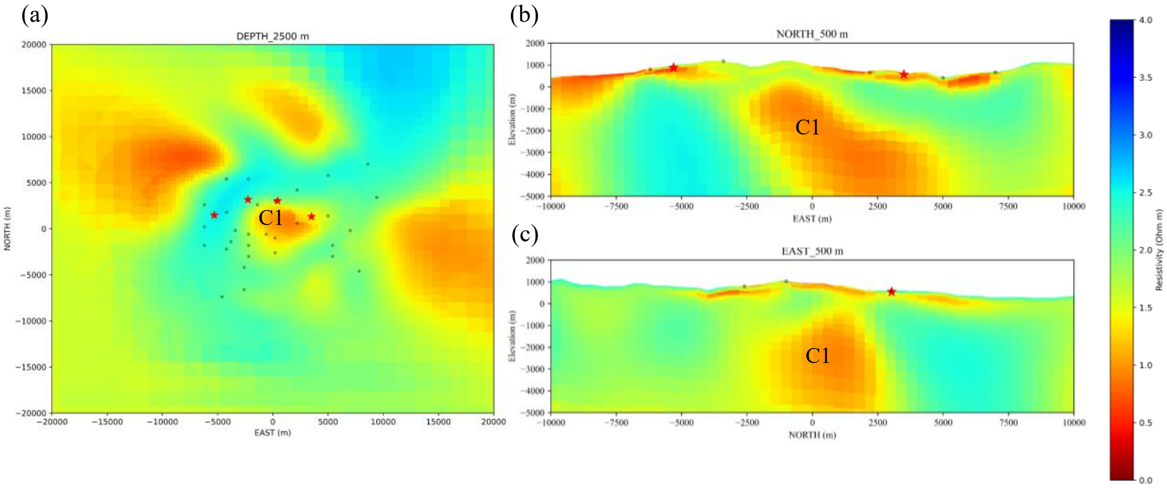

Figure 6

Cross-sections of the average resistivity model: (a) horizontal slice at a depth of 2500 m, (b) vertical cross-section in the north–south direction at x = 500 m, and (c) vertical cross-section in the east–west direction at y = 500 m. C1 and R1 indicate the conductive and resistive regions, respectively. Black dots represent MT observation sites, and red stars denote geothermal power plants that are either in operation or under construction.

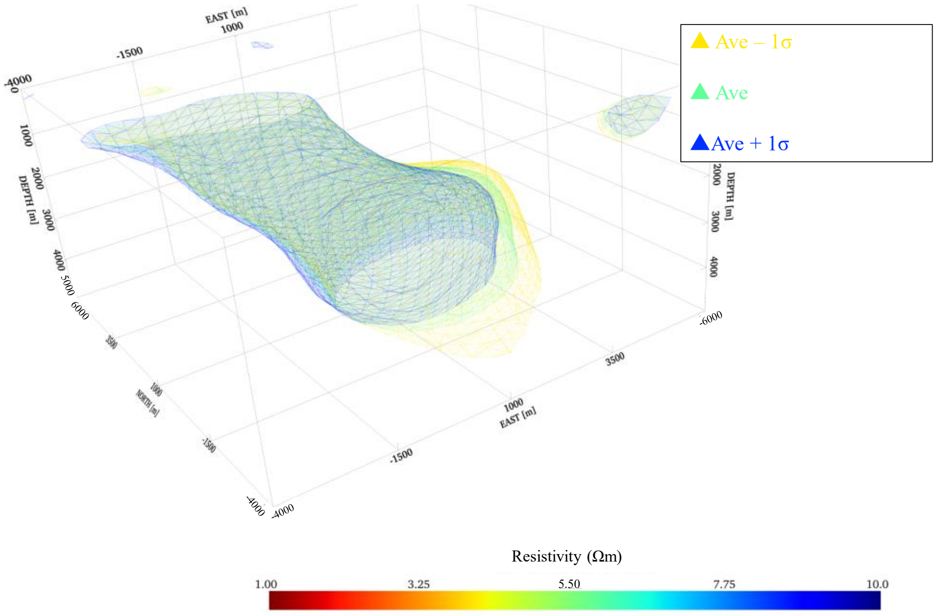

Figure 7

Three-dimensional isosurfaces for the ensemble-average and ±1σ models. Isosurface colors (jet colormap) encode the case-specific minimum resistivity ρ_{min} , evaluated over the analysis domain; for the three representative cases shown, the contours are yellow (ρ_{min} = 4.0 Ω·m; average -1σ), green (ρ_{min} = 5.8 Ω·m; average), and blue (ρ_{min} = 8.4 Ω·m; average +1σ). The isosurface values to plot each case are 12.7, 18.4, 26.7 Ω·m for average -1σ, average, and average +1σ cases, respectively.

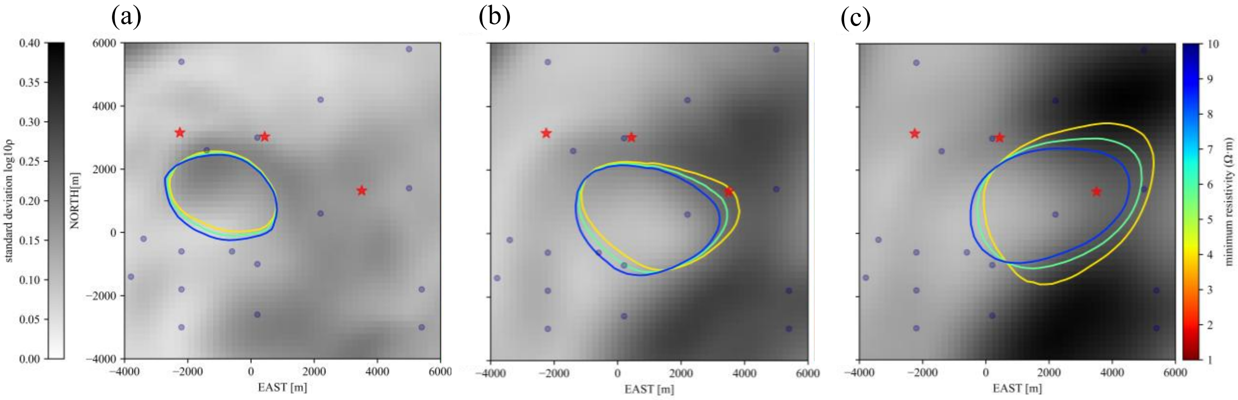

Figure 8

Plan-view contours at depths of (a) 1000 m, (b) 2500 m, and (c) 4000 m for the ensemble average and average ±1σ models. Blue circles denote MT observation sites, and red stars mark geothermal power plants currently in operation or under construction. The grayscale background shows the per-cell standard deviation of resistivity in $\log_{10}$ scale. Line colors (jet colormap) encode the case-specific minimum resistivity ρ_{min} , evaluated over the analysis domain; for the three representative cases shown, the contours are yellow (average -1σ), green (average), and blue (average +1σ).

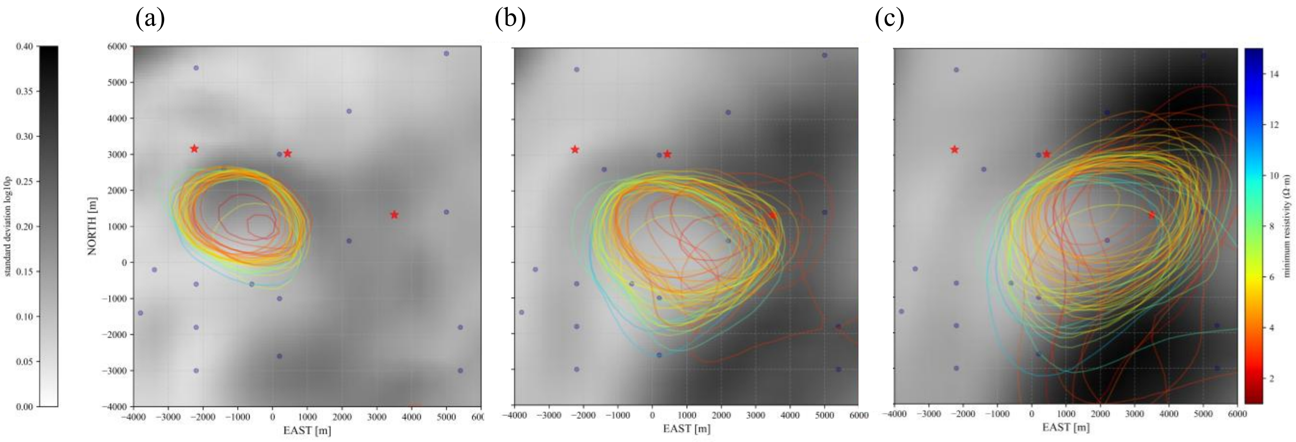

Figure 9

Cross-sections of the contours at depths of (a) 1000 m, (b) 2500 m, and (c) 4000 m for each realization. The other symbols are the same as in Figure 8.

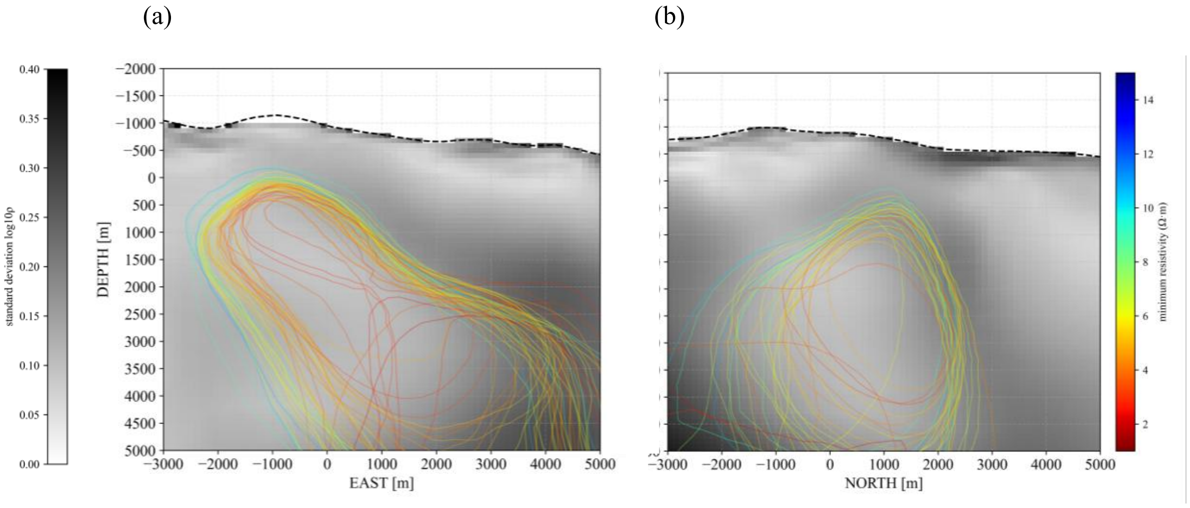

Figure 10

Cross-sections of contours at (a) X = 500 m and (b) Y = 500 m. The others are the same as in Figure 8 and Figure 9.

Data Availability

The inversion codes used in this study are openly available at GitHub: https://github.com/SuzukiAtsushi19911107/FV3DMT.

The MT dataset analyzed here was originally collected by Ishizu et al. (2022) in the Yuzawa geothermal field. The dataset can be downloaded from https://ds.iris.edu/spud/emtf. The other data supporting the findings of this study is available from the corresponding author, upon reasonable request.

Declaration of Competing Interest

The authors declare no known competing financial interests or personal relationships that could have appeared to influence the work reported in this paper.

Funding

This research did not receive any specific grant from funding agencies in the public, commercial, or not-for-profit sectors.

Use of Generative AI

During manuscript preparation, the authors used ChatGPT (OpenAI) solely language editing and refinement of text (grammar, style, and concision). No AI tools were used to generate, analyze, or interpret data, and no AI-generated images were used. After using the tool, the author reviewed and edited the content and takes full responsibility for the content of this publication.

Acknowledgements

We thank colleagues for helpful discussions and the team who acquired and published the Yuzawa MT dataset (Ishizu et al., 2022). We also acknowledge computing resources provided by our institution. This is a preprint and has not been peer-reviewed

References

Causse, E. (2023). Ensemble scenario-based inversion: A new approach for estimating the uncertainty of resistivity models derived from 3D controlled source electromagnetic data. *Geophysical Prospecting*, *71*(5), 847–875. https://doi.org/10.1111/1365-2478.13351

Doherty, J. E., Fienen, M. N., & Hunt, R. J. (2011). *Approaches to Highly Parameterized Inversion: Pilot-Point Theory, Guidelines, and Research Directions Scientific Investigations Report 2010-5168*. https://doi.org/10.3133/sir20105168

Geospatial Information Authority of Japan (GSI). (2025). *Fundamental Geospatial Data: Digital Elevation Model (DEM), 10 m mesh*. https://service.gsi.go.jp/kiban/

Ichihara, H., Sakanaka, ya, Mishina, M., Uyeshima, M., Nishitani, T., Ogawa, Y., Yamaya, Y., Mogi, T., Amita, K., & Miura, T. (2014). *A 3-D electrical resistivity model beneath the focal zone of the 2008 Iwate-Miyagi Nairiku earthquake (M 7.2)*. http://www.earth-planets-space.com/content/66/1/50

Ichiki, M., Kaida, T., Nakayama, T., Miura, S., Yamamoto, M., Morita, Y., & Uyeshima, M. (2021). Magma reservoir beneath Azumayama Volcano, NE Japan, as inferred from a three-dimensional electrical resistivity model explored by means of magnetotelluric method. *Earth, Planets and Space*, *73*(1). https://doi.org/10.1186/s40623-021-01451-y

Ishizu, K., Ogawa, Y., Nunohara, K., Tsuchiya, N., Ichiki, M., Hase, H., Kanda, W., Sakanaka, S., Honkura, Y., Hino, Y., Seki, K., Tseng, K. H., Yamaya, Y., & Mogi, T. (2022). Estimation of Spatial Distribution and Fluid Fraction of a Potential Supercritical Geothermal Reservoir by Magnetotelluric Data: A Case Study From Yuzawa Geothermal Field, NE Japan. *Journal of Geophysical Research: Solid Earth*, *127*(2). https://doi.org/10.1029/2021JB022911

Iwamori, H., Ueki, K., Hoshide, T., Sakuma, H., Ichiki, M., Watanabe, T., Nakamura, M., Nakamura, H., Nishizawa, T., Nakao, A., Ogawa, Y., Kuwatani, T., Nagata, K., Okada, T., & Takahashi, E. (2021). Simultaneous Analysis of Seismic Velocity and Electrical Conductivity in the Crust and the Uppermost Mantle: A Forward Model and Inversion Test Based on Grid Search. *Journal of Geophysical Research: Solid Earth*, *126*(9). https://doi.org/10.1029/2021JB022307

Kelbert, A., Meqbel, N., Egbert, G. D., & Tandon, K. (2014). ModEM: A modular system for inversion of electromagnetic geophysical data. *Computers and Geosciences*, *66*, 40–53. https://doi.org/10.1016/j.cageo.2014.01.010

Macferrin, M., Amante, C., Carignan, K., Love, M., & Lim, E. (2025). The Earth Topography 2022 (ETOPO 2022) global DEM dataset. *Earth System Science Data*, *17*(5), 1835–1849. https://doi.org/10.5194/essd-17-1835-2025

Manassero, M. C., Afonso, J. C., Zyserman, F., Zlotnik, S., & Fomin, I. (2020). A reduced order approach for probabilistic inversions of 3-D magnetotelluric data I: general formulation. *Geophysical Journal International*, *223*(3), 1837–1863. https://doi.org/10.1093/gji/ggaa415

Matsunaga, Y., & Kanda, W. (2025). Critical Factors That Control Hydrothermal Circulation Within Active Volcanoes: Constraints From Numerical Simulation

Based on a Resistivity Structure Model. *Journal of Geophysical Research: Solid Earth*, *130*(2). https://doi.org/10.1029/2024JB029833

Muñoz, G., & Rath, V. (2006). Beyond smooth inversion: The use of nullspace projection for the exploration of non-uniqueness in MT. *Geophysical Journal International*, *164*(2), 301–311. https://doi.org/10.1111/j.1365-246X.2005.02825.x

NOAA National Centers for Environmental Information. (2022). *ETOPO 2022 15 Arc-Second Global Relief Model*. NOAA National Centers for Environmental Information. https://doi.org/10.25921/fd45-gt74

Ogawa, Y., Honkura, Y., Ohtani, F., Kuroki, H., & Mitsuhata, Y. (1997). Preliminary Magnetotelluric Modeling in the Nikko Volcanic Area-Potential Break of Fluid Trap by Volcanic Intrusion. In *J. Geomag. Geoelectr* (Vol. 49).

Pace, F., Martí, A., Queralt, P., Santilano, A., Manzella, A., Ledo, J., & Godio, A. (2022). Three-Dimensional Magnetotelluric Characterization of the Travale Geothermal Field (Italy). *Remote Sensing*, *14*(3). https://doi.org/10.3390/rs14030542

Páll Hersir, G., Árnason, K., & Vilhjálmsson, A. M. (2013). 3D inversion of magnetotelluric (MT) resistivity data from Krýsuvík high temperature geothermal area in SW Iceland. *PROCEEDINGS, Thirty-Eighth Workshop on Geothermal Reservoir Engineering*.

Robertson, K., Thiel, S., & Meqbel, N. (2020). Quality over quantity: on workflow and model space exploration of 3D inversion of MT data. *Earth, Planets and Space*, *72*(1). https://doi.org/10.1186/s40623-019-1125-4

Rung-Arunwan, T., Siripunvaraporn, W., & Utada, H. (2022). The effect of initial and prior models on phase tensor inversion of distorted magnetotelluric data. *Earth, Planets and Space*, *74*(1). https://doi.org/10.1186/s40623-022-01611-8

Sasaki, Y. (2004). Three-dimensional inversion of static-shifted magnetotelluric data. In *Earth Planets Space* (Vol. 56).

Siripunvaraporn, W., Egbert, G., Lenbury, Y., & Uyeshima, M. (2005). Three-dimensional magnetotelluric inversion: Data-space method. *Physics of the Earth and Planetary Interiors*, *150*(1-3 SPEC. ISS.), 3–14. https://doi.org/10.1016/j.pepi.2004.08.023

Suzuki, A. (2025). Development of a three-dimensional magnetotelluric inversion program considering topography with cell-centered finite volume method. *Earth Science Informatics*, *18*(1). https://doi.org/10.1007/s12145-024-01666-z

Takakura, S., & Nakayama, K. (2017). Construction of electric properties database of rocks for metal exploration. *Proceedings of the SEGJ Conference*, *136*, 255–258.

Usui, Y. (2015). 3-D inversion of magnetotelluric data using unstructured tetrahedral elements: Applicability to data affected by topography. *Geophysical Journal International*, *202*(2), 828–849. https://doi.org/10.1093/gji/ggv186

Usui, Y., Uyeshima, M., Hase, H., Ichihara, H., Aizawa, K., Koyama, T., Sakanaka, S., Ogawa, T., Yamaya, Y., Nishitani, T., Asamori, K., Ogawa, Y., Yoshimura, R., Takakura, S., Mishina, M., & Morita, Y. (2024). Three-Dimensional Electrical Resistivity Structure Beneath a Strain Concentration Area in the Back-Arc Side of the Northeastern Japan Arc. *Journal of Geophysical Research: Solid Earth*, *129*(5). https://doi.org/10.1029/2023JB028522

Witter, J. B., Trainor-Guitton, W. J., & Siler, D. L. (2019). Uncertainty and risk evaluation during the exploration stage of geothermal development: A review. *Geothermics*, *78*, 233–242. https://doi.org/https://doi.org/10.1016/j.geothermics.2018.12.011

Yokoi, K., Negi, T., Shimizu, S., Feng, G., Xu, T., & Todaka, N. (2025). Potential supercritical geothermal resources characterised by numerical modelling of fluid flow and heat transport in the Yuzawa area, Akita, Japan. *Geothermics*, *131*, 103355. https://doi.org/10.1016/J.GEOTHERMICS.2025.103355

Zhang, T., Li, J., Ding, W., Kong, F., Fang, Y., Niu, X., Jiang, J., Yu, Z., Tan, P., Shen, Z., Yang, C., Sun, Q., Lu, Z., Yang, B., Liu, Y., Wang, Y., & Zhao, Y. (2025). Magnetotelluric evidence for highly focused mantle melting along the ultraslow-spreading Gakkel Ridge, Arctic Ocean. *National Science Review*, *12*(5). https://doi.org/10.1093/nsr/nwaf077